



Competitive adsorption: Inhibiting the hydroxyl poisoning effect on lattice-confined Ru atoms in metal carbides nanoislands for boosting hydrogen production

Xinyu Chen^a, Chuntao Chen^{a,*}, Majeed Muhammad Amjad^a, Dongping Sun^{a,*}, Bianjing Sun^{a,*}, Kai Zhang^b

^a School of Chemistry and Chemical Engineering, Nanjing University of Science and Technology, 200 Xiao Ling Wei Street, Nanjing 210094, China

^b Sustainable Materials and Chemistry, Department of Wood Technology and Wood-based Composites, University of Göttingen, Büsgenweg 4, 37077 Göttingen, Germany

ARTICLE INFO

Keywords:

Competitive adsorption
Lattice-confined
Nanoislands
Ru/WC_x
Hydrogen production

ABSTRACT

Ruthenium (Ru)-based electrocatalysts are regarded as promising for applications in hydrogen evolution reactions (HER) due to their suitable metal-hydrogen (M-H) bonding energy. However, the strong affinity for adsorbed hydroxyl groups (OH_{ad}) leads to the inactivation of Ru active sites, leading to unsatisfactory performance in practical HER applications. Herein, a competitive adsorption strategy for the design of crystalline lattice-confined atomic Ru in Tungsten Carbide Nanoislands is reported. Benefiting from the unique "island-multi-atoms" structural features, Ru/WC_x exhibits ultra-high mass activity (6000 mA mg⁻¹) and excellent turnover frequency (3.89 H₂⁻¹) at -100 mV vs. RHE, which is 9.5 and 51.2 times higher than commercial 20% Pt/C, respectively. In-depth mechanistic analysis demonstrates that the strength of Ru-OH_{ad} is regulated by the oxophilicity of W atoms and the stronger W-OH_{ad} bond to alleviate Ru site inactivation, thus enhancing the HER activity. This strategy provides a novel concept for designing advanced catalysts.

1. Introduction

Actively addressing climate change has become a global consensus, and green carbon reduction has become one of the main themes of global economic development [1–4]. Electrochemical water splitting is considered a reliable technology via exiting traditional fossil fuels ear towards a sustainable green hydrogen energy system [5–9]. Electrocatalysts for alkaline media have attracted significant attention due to their lower corrosion than in acidic media [10–14]. In alkaline conditions, the HER performance of electrocatalysts primarily depends on the dissociation of H₂O, which leads to the formation of adsorbed hydroxyl species (OH*) and hydrogen ions (H*) via the Volmer step, followed by the combination of H* to form molecular hydrogen (H₂) through either the Heyrovsky or Tafel step [15,16]. Thus far, vast alkaline HER electrocatalysts were designed to overcome kinetic barriers that occurred in the HER reaction process by optimizing H₂O dissociation and hydrogen adsorption [13,17–19]. The limitation of OH_{ad} transfer in the Volmer reaction derived from strong adsorption between the active site and OH_{ad} can limit the overall HER activity but has received little attention

[20–22]. Therefore, collaborative optimization of H₂O adsorption and dissociation capabilities is crucial for designing highly efficient alkaline HER catalysts.

In recent years, ruthenium (Ru) has emerged as a promising alternative to platinum (Pt)-based electrocatalysts for the HER due to the following reasons: (i) comparable H₂O dissociation rates to Pt (enhances the rate of the Volmer reaction) [23,24], (ii) the rapid adsorption of H protons is facilitated by the strong metal-hydrogen (M-H) bonds [25–27], (iii) low price (1/3 Pt) [28] and resistance to corrosion in alkaline media [29]. However, the HER performance of ruthenium (Ru)-based electrocatalysts in alkaline media remains suboptimal. The strong Ru-OH bond leads to the poisoning of the Ru active site necessary for H₂O dissociation, consequently impacting the Volmer step in alkaline media and ultimately restricting the overall HER activity [30–32]. Therefore, weakening the Ru-OH bond strength is significant for the advancement of highly efficient alkaline Ru-based HER electrocatalysts.

Dispersing catalytically active metals to the atomic level on a carrier (preparation of single atom catalysts) with an individual specific function to integrate each component is a viable approach [33–37].

* Corresponding authors.

E-mail addresses: chchunt@njust.edu.cn (C. Chen), sundpe301@163.com (D. Sun), bjsun1992@163.com (B. Sun).

<https://doi.org/10.1016/j.apcatb.2023.123644>

Received 10 September 2023; Received in revised form 4 December 2023; Accepted 17 December 2023

Available online 19 December 2023

0926-3373/© 2023 Elsevier B.V. All rights reserved.

Transition metal carbides typically have high stability, chemical resistance, and metal-like electrical conductivity [38,39]. Tungsten carbide is widely used in the study of alkaline HER electrocatalysts due to its similar electronic density of states at the Fermi energy level to Pt [40–43]. However, Ru atoms are more inclined to form clusters attached to the surface of tungsten carbide under high-temperature treatment due to its greater cohesion energy, which may ultimately affect the HER behavior of the active site [44–46]. Hence, confining the Ru atoms within the tungsten carbide lattice to achieve outstanding HER performance remains a significant challenge.

To address the above challenges, we present here an efficient HER catalyst with transition metal carbide nanoislands loaded with Ru single atoms stranded on a 'micro-sea' of amorphous carbon (Ru/WC_x). The Ru atoms are strictly confined within the WC_x lattice and cross-island migration is effectively curbed, which can greatly accelerate the regeneration of Ru active sites. Moreover, the 'Pt-like' d-band electron density state of WC_x leads to preferential adsorption of OH_{ad} at the W site. The synergistic interaction between WC_x nanoislands and Ru single atoms provides significant advantages, the Ru/WC_x catalyst exhibited a ultralow overpotential of 29 mV (10 mA cm⁻²) and a lower Tafel slope of 43 mV dec⁻¹ in 1 M KOH. The WC_x substrate reduces the hydrolysis energy barrier while alleviating the hydroxyl poisoning effect of the Ru active site, thus providing a 9.5 times higher mass activity and 51.5 times higher turnover frequency (6000 mA mgRu⁻¹ and a turnover frequency of 3.89 s⁻¹ at -100 mV vs RHE) than commercial Pt/C. Subsequently, we assessed the catalytic activity of the developed Ru/WC_x in alkaline seawater, and the results demonstrated its exceptional performance and stability. Furthermore, experimental and theoretical analyses are provided in detail how the designed structure suppresses the hydroxyl poisoning during HER in an alkaline solution. This paper also presents novel insights into the rational design of catalysts for complex reactions involving competitive adsorption of intermediates.

2. Materials and methods

2.1. Chemical reagents and materials

Dopamine hydrochloride, ruthenium chloride hydrate (RuCl₃·xH₂O, Ru content of ~47%), commercial Pt/C catalyst (Pt content of 20%), Facion 117 solution (5%), and potassium hydroxide (KOH, 95%) were obtained from Shanghai Aladdin Biochemist Technology Co., LTD. Tungstic acid sodium salt dihydrate (Na₂WO₄·2 H₂O, 95%), hydrochloric acid (HCl, 36.5%) was obtained from Sinopharm Chemical Reagent Co., China. Unless otherwise specified, all chemicals were used as received without additional purification. All aqueous solutions were prepared with DI water.

2.2. Experimental sections

Initially, 2.5 mmol (0.474 g) of dopamine hydrochloride (DA) was dissolved in 25 mL of water, yielding a 0.1 M solution of dopamine in water. The pH of the dopamine solution was lowered to approximately 2 by adding HCl. Subsequently, RuCl₃·xH₂O was added to the DA solution and thoroughly stirred. After that, a slow dropwise addition of 25 mL of sodium tungstate solution (containing 2.5 mmol of Na₂WO₄·2 H₂O) was performed into the DA-Ru solution. The reaction mixture was stirred for an additional hour, followed by collection of the product (DW-Ru) through centrifugation. The collected product was subsequently washed three times with deionized (DI) water and ethanol. The products were dried overnight at 60 °C in an oven to obtain the DW-Ru precursor. Subsequently, the DW-Ru precursor was subjected to carbonization in an argon furnace at various temperatures (800 °C, 900 °C, and 1000 °C) for 2 h using a ramp rate of 2 °C per minute. The final black powder was donated as Ru/wi_{cks}. As a comparison, the effect of Ru content on HER performance was investigated by varying the RuCl₃·xH₂O (0.025, 0.125, and 0.5 mmol) addition, and the synthesis process was similar to the

preparation of Ru/Wa_{cks}.

2.3. Characterizations

X-ray diffraction (XRD) analysis using Bruker-AXS D8 Advance with Cu K α radiation was performed to determine the crystalline nature of the as-prepared samples. X-ray photoelectron spectroscopy (XPS) with Thermo Fisher Scientific Nexsa using Al K α radiation was employed to identify the chemical compositions. The peaks were calibrated according to the standard position of the C 1 s peak (284.8 eV). The morphology of the prepared materials was observed using scanning electron microscopy (SEM) with JSM-7800 F PRIME and transmission electron microscopy (TEM) with FEI, Tecnai F20. The concentration of doped Ru in the sample was determined using inductively coupled plasma (ICP) with an Agilent 5110 instrument. A Renishaw inVia™ Raman spectrometer, with an excitation wavelength of 532 nm was used to characterize the degree of order and graphitization. Thermogravimetric analysis (TGA) was conducted in N₂ conditions from room temperature to 1000 °C, with a rapid of 10 °C/min (TA, TGA5500). N₂ sorption analysis was conducted on a Micromeritics ASAP 2460 instrument. The X-ray absorption spectra (XAS) including X-ray absorption near-edge structure (XANES) and extended X-ray absorption fine structure (EXAFS) of the samples at Ru k-edge were collected at the Shanghai Synchrotron Radiation Facility (SSRF) center, the Ru k-edge XANES data were recorded in a transmission mode. Ru foil and RuO₂ were used as references. Data reduction, data analysis, and EXAFS fitting is applied through Athena and Artemis software. Wavelet transformation (WT) is also employed using the software package developed by Funke and Chukalina using Morlet wavelet with $\kappa = 10$, $\sigma = 1$.

2.4. Electrochemical measurements

The electrocatalytic hydrogen production (HER) test adopts a three-electrode test system with a carbon rod as the counter electrode and electrochemical workstation model CorrTest CS2350H to evaluate its catalytic activity. The reference electrode employed in both 1 M KOH and 1 M KOH seawater solutions is the Hg/HgO reference electrode. To prepare the electrode, 10 mg of Ru/WC_x catalyst was dispersed in a mixture of 100 μ L of 5 wt% Nafion solution and 900 μ L of ethanol using sonication for over 30 min. Subsequently, 10 μ L of the resulting suspension was drop-cast onto a 4 mm glassy carbon electrode, and air-dried to create a working electrode with a loading of 0.80 mg/cm⁻². All the measured potentials were converted to the potential vs the reversible hydrogen electrode (RHE) according to the Nernst equation:

$$E_{\text{RHE}} = E_{\text{Hg/HgO}} + 0.098 + 0.059\text{pH} \quad (1)$$

where E_{RHE} describes the experimentally measured potential and $E_{\text{Hg/HgO}}$ denotes the standard potential of saturated mercury-mercuric oxide electrode.

Linear Scanning Voltammetry (LSV) curves are scanned at 5 mV s⁻¹ to minimize background current, and 20 cyclic voltammetry (CV) tests to stabilize the current. A 95% iR-compensation (~4.5 Ω) was applied to all the LSVs. The electrochemical surface areas (ECSA) were evaluated by CV curves at the potential window of 0.27 to 0.37 V vs. RHE with different scan rates of 20, 40, 60, 80, 100 and 120 mV s⁻¹, respectively. Electrochemical impedance spectroscopy (EIS) was carried out with a potentiostatic EIS method from 100 kHz to 0.1 Hz at a 10 mV overpotential. Chronopotentiometry (CP) was employed to evaluate the stability of the catalysts in all HER tests. CO stripping experiments were conducted at a scan rate of 20 mV s⁻¹ to assess the samples' OH binding capacity. TOF of the catalysts is calculated from the equation: [47].

$$\text{TOF}(\text{s}^{-1}) = \frac{j \times S}{n \times e \times N} (\text{s}^{-1}) \quad (2)$$

In the equation, j represents the current density (A cm⁻²), S denotes

the surface area of the electrode (cm^2), n corresponds to the number of electrons involved ($n = 2$ for HER), and e signifies the electric charge carried by a single electron (1.602×10^{-19} C). N represents the number of Ru or Pt atoms on the respective electrode. In this instance, the calculated value serves as a lower limit for the turnover frequency (TOF) [48].

2.5. Calculation methods

The present study employs the density functional theory (DFT)-based projection augmentation wave (PAW) method for conducting first-principles calculations[49]. The description of core electrons employed the projector augmented wave (PAW) method, while the exchange-correlation energy was computed using the generalized gradient approximation (GGA) within the Perdew-Burke-Ernzerhof (PBE) functional[50]. The WC_x surface was generated by stochastic removal of carbon (C) atoms from the surface of the WC crystal. A cut-off energy of 450 eV is used for optimizing the calculations of atoms and cell crystal. For accelerated convergence during optimization, a Monkhorst-Pack ($3 \times 3 \times 1$) k-point grid was utilized, and the force, energy-convergence criterion for self-consistent field (SCF) were set to 1×10^{-5} eV and $0.05 \text{ eV } \text{\AA}^{-1}$, respectively. In all calculations, the DFT+D3 method was utilized to incorporate the van der Waals (vdW) correction[51]. In order to ensure complete geometry relaxation, a vacuum space of 15 \AA was added along the z-axis. The climbing-image nudged-elastic-band (CI-NEB) method was employed to search for transition states, with a force convergence criterion set at $0.03 \text{ eV}/\text{\AA}$. Finally, the spin polarization was considered in all calculations. The free energies were calculated using the following equation:

$$\Delta G = \Delta E + \Delta \text{ZPE} - \Delta \text{TS} \quad (3)$$

where ZPE represents the change in zero-point vibrational enthalpy, and TS denotes the entropy. The OH binding energies are calculated as:

$$E(\text{M-OH}) = E(\text{M-OH}) - E(\text{M}) - [E(\text{H}_2\text{O}) - 0.5E(\text{H}_2)] \quad (4)$$

where $E(\text{M-OH})$ is the total energy of the M-OH film, $E(\text{M})$ is the energy of M without an OH, and $E(\text{H}_2\text{O})$ and $E(\text{H}_2)$ are the energies of H_2O and H_2 in gas phase.

3. Results and conclusions

3.1. Synthesis and crystal characterization

Ru/WC_x was synthesized via a facile approach as illustrated in Fig. 1a. First, 0.1 M dopamine (DA) solution and a quantity of RuCl_3 are mixed to form a DA-Ru solution. Then, an equal amount of 0.1 M $\text{Na}_2(\text{WO}_4)_2 \cdot 2\text{H}_2\text{O}$ was added dropwise to the DA-Ru solution yielding a yellow-brown metal-organic compound (DW-Ru). The representative scanning electron microscopy (SEM) images reveal that the DW-Ru precursor microspheres are assembled from aggregated nanosheets (Fig. S1). Thermogravimetric analysis (TGA) conducted under N_2 flow revealed substantial weight loss at approximately 400°C and 800°C , with no additional weight loss observed beyond 900°C (Fig. S2). SEM images demonstrate that both carbonized pure WC_x and Ru/WC_x maintain the morphology of microspheres formed from layered nanosheets (Figs. 1b and S3), and the TEM images further confirm this structure (Figs. 1c and S4a). Nitrogen adsorption analysis showed that both the WC_x and Ru/WC_x catalysts exhibited good adsorption, and BET

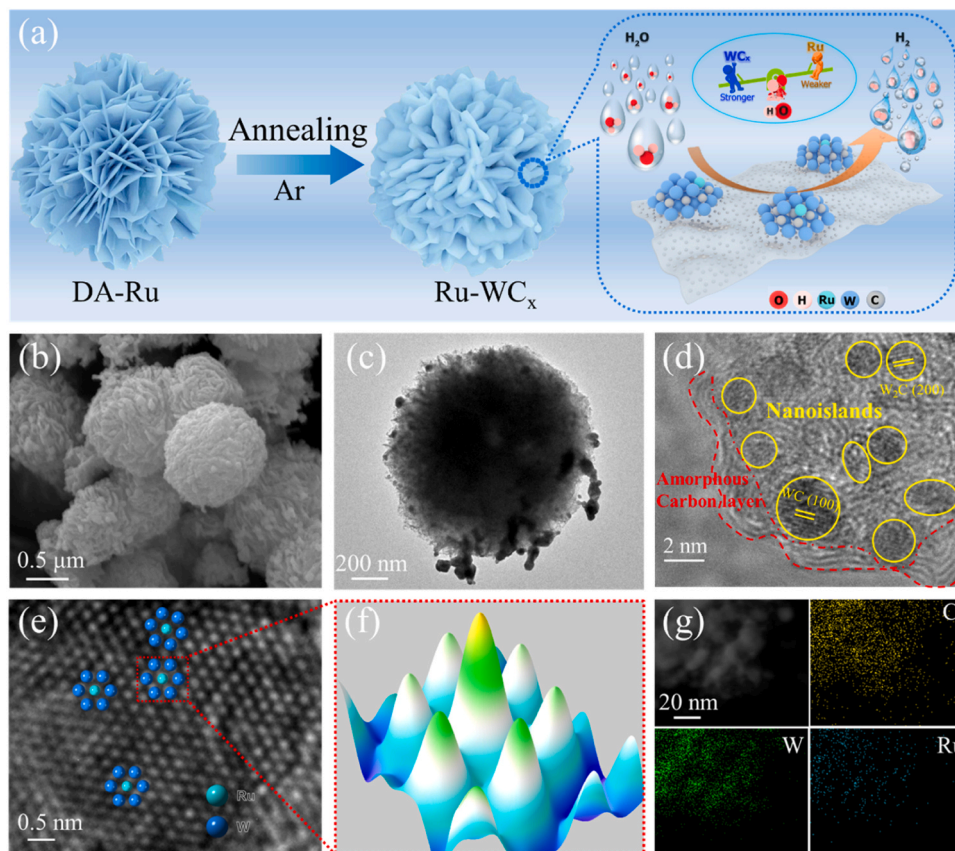


Fig. 1. Synthesis of Ru/WC_x and characterization of crystalline lattice-confined atomic Ru in WC_x nanolands. (a) Schematic illustration for the synthesis of Ru/WC_x . (b) Representative SEM image and (c) TEM image of Ru/WC_x . (d-e) HRTEM images of Ru/WC_x . (f) 3D-scanning intensity profile obtained from the area highlighted with red rectangles in Fig. 1e. (g) EDX mapping of W, C, and Ru elements in Ru/WC_x . (For interpretation of the references to color in this figure legend, the reader is referred to the web version of this article.)

analysis displayed surface areas of 209.6 m²/g and 154.2 m²/g, respectively (Fig. S5). This is primarily attributed to the three-dimensional structure of the carbon matrix, which increases the exposed surface area by providing more accessible active sites for the catalytic reaction.

Notably, high-resolution transmission electron microscopy (HRTEM) images further reveal 2–5 nm Ru/WC_x nanoislands distributed over amorphous carbon “microsea” (Fig. 1d), HADDF-STEM images reconfirmed the structural features (Fig. S6). This continuous graphitized carbon shell can accelerate charge transport and improve active site stability [52]. The lattice stripes with the planar spacing of 0.25 nm and 0.23 nm belong to the WC (100) and WC₂ (200) crystal planes, respectively. As the intensity of HRTEM is inversely proportional to the square of the atomic number *Z*, the brighter spots observed in Fig. 1e should be attributed to the presence of Ru atoms. The 3D intensity distribution of the red selected region in Fig. 1f demonstrates a clear contrast in brightness between the Ru and W sites, indicating that the Ru site possesses a better atomic dispersion on WC_x [13]. Furthermore, the elemental mapping analysis conducted using energy dispersive

spectroscopy (EDS) showed a substantial overlap between the regions of Ru and W atom distribution in the sample (Fig. 1g), further confirming that Ru is uniformly distributed in the WC_x nanoislands. The morphologies of pure WC_x and Ru doped WC_x with diversified content were comprehensively investigated by SEM and TEM, which reveal Ru doping in small quantity had little influence on the microspheres morphologies (Figs. S4b, S7, S8 and S9). The catalysts obtained at 900 °C demonstrated excellent performance in subsequent HER activity tests, and the subsequent discussion will primarily focus on the catalysts treated at 900 °C.

The effect of the doped Ru atoms on the metal carbide crystal structure was further explored by X-ray diffraction (XRD) (Fig. S10). The XRD patterns of both WC_x and Ru/WC_x exhibit similar reflections including hexagonal WC (PDF#72-0090) and orthorhombic WC₂ (PDF#89-2371) phases. Specifically, the diffraction peaks located at 31.5°, 35.6°, and 48.3° are corresponding to the characteristic (1 0 0), (0 0 1) and (1 0 1) crystal planes of WC, respectively. The diffraction peaks at 34.4°, 38.0°, and 61.7° correspond to the typical (0 0 2), (2 0 0), and (0 4 0) crystal planes of WC₂, respectively. Notably, the absence of new

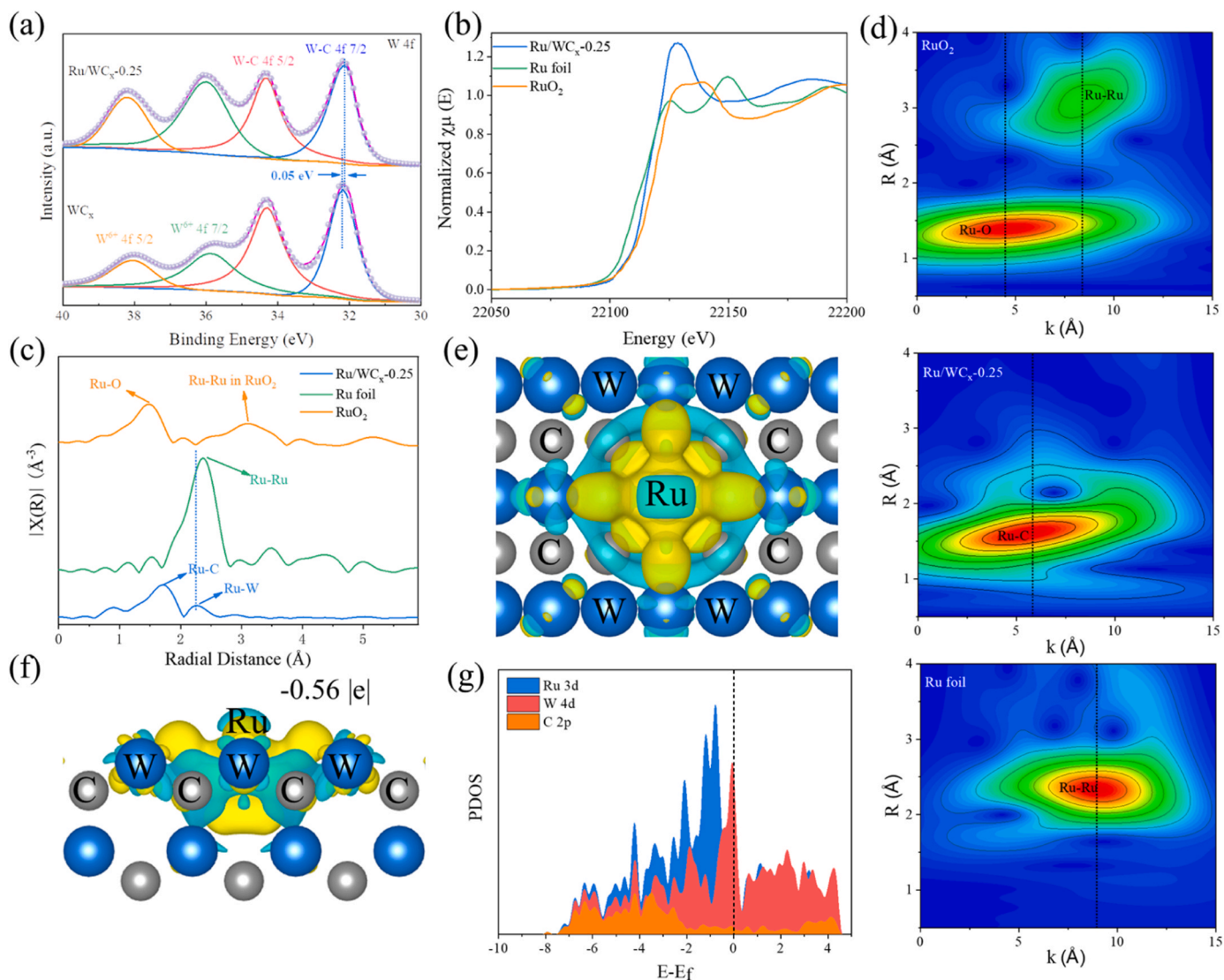


Fig. 2. Chemical states of Ru/WC_x. (a) High-resolution W 4f X-ray photoelectron (XPS) spectra. (b-d) Ru k-edge XANES spectra, Fourier-transform Ru k-edge EXAFS spectra, and wavelet transform for the k³-weighted Ru k-edge EXAFS signals of Ru /WC_x, Ru foil, and RuO₂. (e) Charge density differences of lattice-confined Ru atoms (Ru/WC_x). The yellow region signifies charge accumulation, while the blue region indicates a reduction in charge. (f) The Bader charge analysis of the atomic Ru site. (g) PDOS of W 5d orbitals Ru 4d orbitals and O 2p orbitals in the Ru/WC_x. (For interpretation of the references to color in this figure legend, the reader is referred to the web version of this article.)

diffraction peaks related to the Ru phase demonstrated that Ru species may be distributed as individual atoms or ultra-small nanoparticles. The Raman spectra further verify the presence of the pure WC_x and Ru/WC_x carbon shells and their states based on the D and G bands located at ~ 1353 and 1589 cm^{-1} (Fig. S11). The smaller I_D/I_G ratio (0.67 for WC_x and 0.68 for Ru/WC_x) indicates a higher degree of graphitization of the carbon shell [13]. Furthermore, the peaks at approximately 686 and 807 cm^{-1} are attributed to the W-C stretching vibration [41], while weaker vibration peaks at around 910 and 955 cm^{-1} belong to W=O stretching modes [53]. Such unique structure is conducive to antioxidant enhancements. The presence of the four elements Ru, W, C, and O in the Ru/WC_x with the resulting chemical composition was confirmed by X-ray photoelectron energy spectrum (XPS) (Fig. S12). The precise Ru content of Ru/WC_x was determined to be approximately 1.41 wt% by using inductively coupled plasma (ICP) atomic emission spectroscopy (Table S1). The XPS of W 4f shows that the W 4f_{7/2} spectrum of Ru/WC_x is negatively shifted compared to WC_x , indicating an electron-rich state of W species (Fig. 2a). The presence of Ru elements in Ru/WC_x and their strong interactions with WC_x substrates can be inferred based on the obtained results.

X-ray absorption fine structure spectroscopy (XAFS) was conducted to give vital insight into the chemical state and local coordination

structure of Ru in Ru/WC_x . Fig. 2b presents the Ru K-edge X-ray absorption near-edge structure (XANES) spectra of Ru/WC_x , RuO_2 , and Ru foil. The absorption edge of Ru/WC_x is located between Ru foil and RuO_2 , but is very close to that of RuO_2 , indicating that Ru oxidation occurs after doping with WC_x [54], which is in alignment with the findings derived from XPS. The Fourier transform extended X-ray absorption fine structure (FT-EXAFS) spectra corresponding to Ru/WC_x were employed to explore the bonding configuration of Ru within Ru/WC_x . In Fig. 2c, the main peak of Ru/WC_x is centered at 1.72 Å, which is attributed to the scattering characteristics of Ru-C indicating the presence of a single Ru atom [13]. Additionally, a minor Ru-W peak at approximately 2.23 Å is observed within the same spectrum, which is congruent with the substitutional doping of Ru in the W position. Then, a quantitative curve fitting analysis on the EXAFS spectra of Ru/WC_x was performed to obtain the coordination number of Ru/WC_x . The coordination number of Ru-C of 6.2 is strikingly similar to that of W-C which is 6. This suggests the integration of Ru atoms in the WC_x lattice, taking up the atomic sites originally occupied by W (Fig. S13 and Table S2) [38]. The high-resolution wavelet transform extended x-ray absorption fine structure (WT-EXAFS) analysis in both K and R space further elucidates the dispersion state of Ru species within Ru/WC_x [55]. The pronounced Wavelet Transform (WT) signal at 5.75 Å^{-1} is tied to the

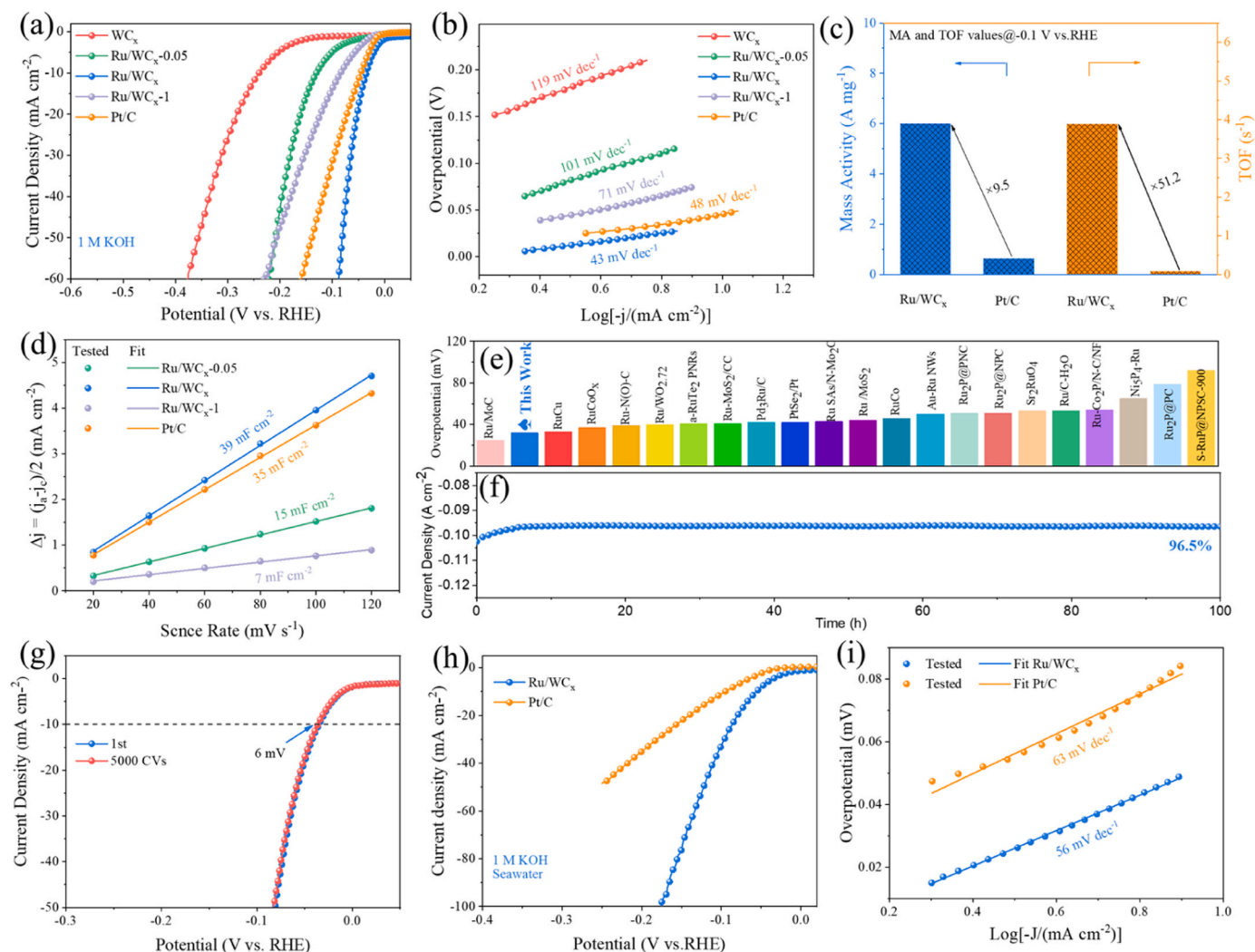


Fig. 3. HER catalytic performances. (a-b) LSV curves and Tafel slope plots for $Ru/WC_x-0.05$, Ru/WC_x , Ru/WC_x-1 , WC_x , and Pt/C in 1.0 M KOH. (c) Comparison mass activity and TOF values for Ru/WC_x and Pt/C at -0.1 V vs. RHE. (d) Plots of the current density versus the scan rate. (e) The comparison involves assessing the overpotentials required for noble metal-based samples to achieve a current density of 0.1 A cm^{-2} in a 1.0 M KOH. (f) The stability curve of Ru/WC_x tested at 100 mA cm^{-2} . (g) LSV curves of Ru/WC_x before and after 5k ADT cycles. (h-i) LSV curves and Tafel slope plots for Ru/WC_x and Pt/C in 1.0 M KOH seawater.

Ru-C path (Fig. 2d). In addition, no signal showing the association with Ru-Ru bonding is present, which implies the atomic dispersion of Ru atoms in Ru/WC_x. Based on HRTEM, XRD and XPS characterization of Ru/WC_x, "nano-islands" of transition metal carbides loaded with Ru atoms have been successfully synthesized. The as-designed Ru/WC_x catalyst consists of three salient features: (1) a robust high surface area amorphous carbon carrier, (2) nano-scale metallic tungsten carbide stably anchored to the carrier as islands, and (3) single or multiple Ru metal atoms (M1) located on these islands.

Density Functional Theory (DFT) calculations are subsequently employed to provide deeper insight into the electronic structure of Ru atoms bound in the WC_x nanoislands. The WC_x surface is simulated by randomly removing C atoms from the WC (100) crystal surface. Ru/wa_x was obtained by using Ru atoms to replace the W positions on the wicks surface. We first calculated the charge density difference (CDD) of Ru/WC_x, where the lattice-limited Ru atom and the surrounding W atom exhibit a clear charge separation between them, while the charge is uniformly distributed around the Ru atom (Fig. 3e). In addition, the Bader charges of the Ru atoms in Ru (001), RuO₂(001) and Ru/WC_x were calculated, and the results showed that the $-0.56|e|$ of the Ru atoms in Ru/WC_x is located between metal Ru and RuO₂ (Fig. 3f, Fig. S14). This result further indicates that the valence state of the Ru atom in Ru/WC_x is between 0 and 4+, which is consistent with the results of the XAFS analysis. More importantly, the unique WC_x surface effectively stabilizes the low valence state of Ru atoms, thus optimizing H₂O molecule and H adsorption. Furthermore, the partial density of states (PDOS) shows that Ru 3d and W 4d, C 2p orbital energy levels are well matched and show significant bonding below the Fermi energy level. The shorter C-Ru bond can confine the Ru atoms in the WC_x lattice, thereby promoting the stability of the catalyst HER process (Fig. 2g).

3.2. HER performance analysis

The HER activities of the synthesized samples and Pt/C were investigated in 1.0 M KOH electrolyte involving a three-electrode system. Fig. 3a records the typical linear sweep voltammetry (LSV) curves of the as-prepared catalysts. Pristine WC_x catalyst exhibited rather poor HER performance. Conversely, among all catalysts, Ru/WC_x demonstrated superior HER performance. Specifically, Ru/WC_x requires a fairly low overpotential of 29 mV to achieve a current density of 10 mA cm⁻², which is significantly better than Pt/C (38 mV), Ru/WC_x-0.05 (130 mV), Ru/WC_x-1 (84 mV) and WC_x (240 mV) (Fig. S15). For Ru/WC_x-0.05 and Ru/WC_x-1 activities lower than Ru/WC_x, it can be assumed that lower concentrations of Ru atoms, are not sufficient to provide enough active sites, whereas high concentrations of Ru atoms lead to the formation of nanoclusters, which in turn reduces the catalytic activity [56,57]. Tafel analysis was further performed to deepen understanding of reaction microkinetics. As showed in Fig. 3b, the slopes of WC_x, Ru/WC_x-0.05, and Ru/WC_x-1 were 119, 101, and 79 mV dec⁻¹, respectively. Moreover, Ru/WC_x exhibits an extremely low Tafel slope of 43 mV/dec⁻¹, outperforming even Pt/C, which has a Tafel slope of 48 mV/dec⁻¹. A smaller Tafel slope implies a faster electron transfer rate and H₂ production rate [55,58]. Measurements obtained through electrochemical impedance spectroscopy (EIS) have shown that the charge transfer resistance associated with Ru/WC_x is less than that of Pt/C, Ru/WC_x-0.05, Ru/WC_x-1, and WC_x (Fig. S16). This results further demonstrates the best HER kinetics of Ru/WC_x. Furthermore, to examine the characteristics of Ru/WC_x more accurately, mass activity and turnover frequency (TOF) of the noble metal were computed using Pt/C as a benchmark. The mass activity and TOF values of Ru/WC_x at -100 mV overpotential are 6000 mA mg⁻¹ and 3.89 H₂⁻¹, which are 9.5 and 51.2 times higher than those of commercial Pt/C (630 mA g⁻¹ and 0.076 H₂⁻¹), respectively (Figs. 3c, S17 and S18). Higher mass activity and TOF values indicate a high intrinsic activity. The electrochemical surface area (ECSA) was roughly evaluated by the bilayer capacitance (C_{dl}) [59]. The C_{dl} of Ru/WC_x is over than that of WC_x-0.05 and WC_x-1,

indicating that a suitable content of Ru atoms confined within the WC_x lattice is advantageous in augmenting the C_{dl} of the catalyst (Fig. 3d and S19). Subsequently, we contrasted the HER overpotential of numerous recently reported Ru-based catalysts, and the results revealed that Ru/WC_x ranks among the one of the best HER catalysts in alkaline solutions (Fig. 3e and Table S3).

The durability of a catalyst is a crucial metric in assessing the applicability potential of HER catalysts. Therefore, the Ru/WC_x catalysts were subjected to tests at a constant current flow of 100 mA cm⁻². After 100 h of testing, its current density can be maintained at 96.5% (Fig. 3f). In addition, inductively coupled plasma mass spectrometry (ICP-MS) was used to characterize the post-test solutions (Tables S4), which showed that Ru did not undergo a significant solution, which can be attributed to the protection of the carbon layer. After 5000 CV, the overpotential of Ru/WC_x increased by only 6 mV further demonstrating its stability (Fig. 3g). After HER stability tested, the structural stability of Ru/WC_x was tracked using XRD and XPS. As can be seen from Fig. S20, the corresponding feature peaks of WC_x are well preserved after the stability test. The high-resolution XPS results also demonstrate that the valence states of W and Ru are not significantly elevated after the test (Fig. S21). In addition, its unique WC_x nano-island morphology remains largely unchanged, indicating its excellent structural stability (Fig. S22).

To investigate the potential application range of Ru/WC_x, we further examined its HER activity in alkaline seawater (1.0 M KOH seawater). The LSV curves are shown in Fig. 3h. Ru/WC_x continues to exhibit extremely high HER activity, requiring only 56 mV of overpotential to drive a current density of 10 mA cm⁻², which is significantly better than a commercial Pt/C catalyst (95 mV). Furthermore, the Tafel slopes of Ru/WC_x and Pt/C were 56 mV dec⁻¹ and 63 mV dec⁻¹, respectively (Fig. 3i), indicating that they both follow the Volmer-Heyrovsky reaction mechanism of HER in 1.0 M alkaline seawater [23]. Ru/WC_x with a lower Tafel slope suggests a faster HER reaction kinetics. In addition, Ru/WC_x has a mass activity of up to 3640 A g_{Ru}⁻¹ at an overpotential of -100 mV, which is 121 times higher than that of commercial Pt/C, providing greater application advantages (Fig. S23). The I-t curve, employed for the assessment of long-term electrochemical stability, was gauged at a consistent potential of 0.056 V. The current drop of Ru/WC_x was negligible after 40 h of continuous reaction, further confirming its application properties (Fig. S24).

3.3. Understanding the active centers

To gain insight into the active site on Ru/WC_x, thiocyanate ions (SCN⁻), which are considered to be toxic to the metal-centered active site, were added to the electrolyte [54,60]. Obtained results from the poisoning studies suggest that the presence of SCN⁻ significantly diminishes the activity of Ru/WC_x. Specifically, when SCN⁻ was added to the electrolyte, the overpotential of Ru/WC_x to obtain a current density of 10 mA cm⁻² increased by 162 mV, indicating that the Ru active site was blocked (Fig. 4a). Upon identifying the active site, the role of OH_{ad} in the overall reaction process was further explored. Since the OH_{ad} adsorbed on the surface facilitates the oxidation of the adsorbed CO intermediates to CO₂, CO stripping experiments were used to evaluate the ability of the oxidizer to adsorb OH⁻ [61]. As illustrated in Fig. 4b, the starting potential of Ru/WC_x is 0.70 V, while the starting potential of WC_x is ~ 0.66 V. The higher onset potential obtained indicates that Ru/WC_x has a weaker adsorption capacity for OH than WC_x, and it can also indicate that more unblocked active sites are available in Ru/WC_x for promoting the HER reaction. In addition, the different onset potentials also indicate that Ru/WC_x and WC_x have differentially different electronic structures. To gain more insight into the origin of the superior HER activity of Ru/WC_x, the interaction of Ru/WC_x and WC_x with OH⁻ at 1.0 M KOH was investigated using CV curves. As shown in Fig. 4c, Ru/WC_x shows a distinct peak in the adsorption potential interval compared to pristine WC_x, which confirms stronger oxophilicity of WC_x than Ru atoms [20,23,62,63]. The excellent oxophilicity not only

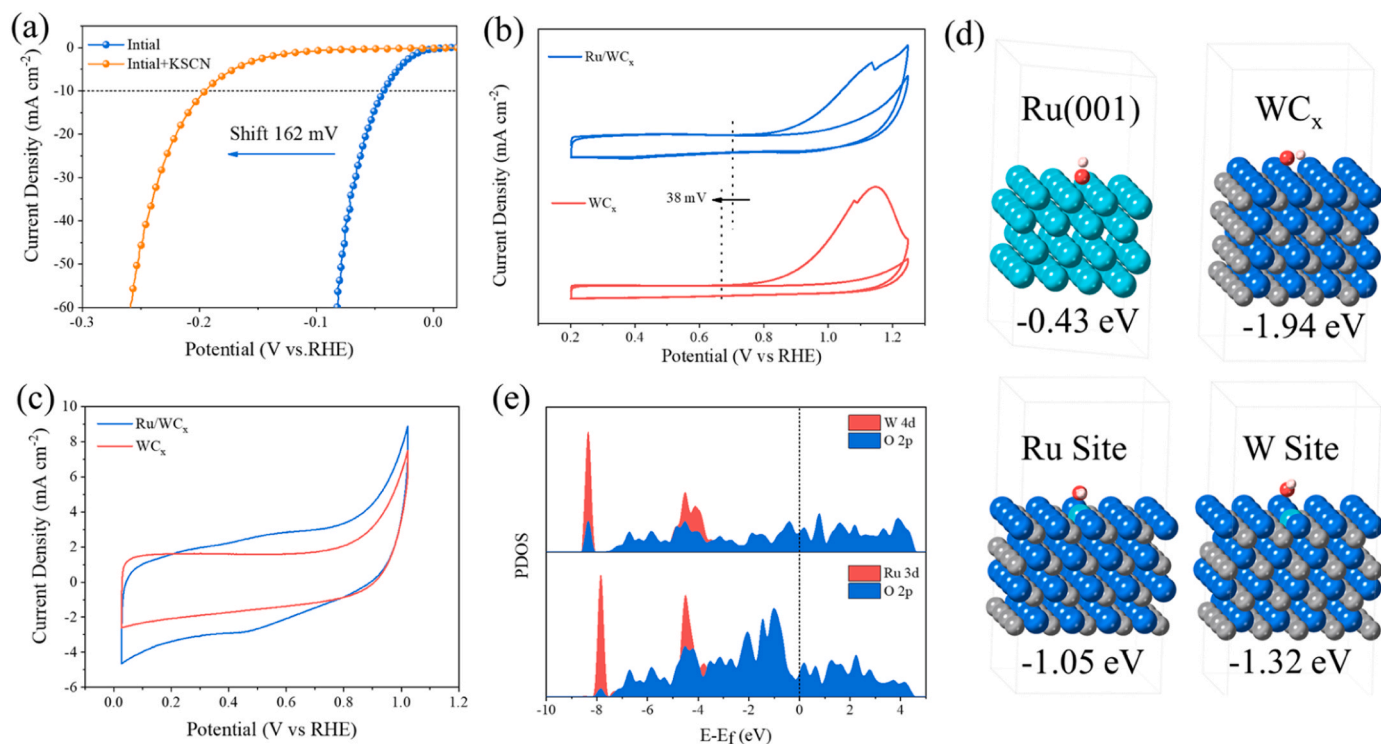


Fig. 4. Understanding the Active Centers. (a) The HER polarization curves of Ru/WC_x poisoned by KSCN (10 mM). (b) CO-stripping voltammograms of catalysts measured in 1.0 M KOH. (c) CV curves of Ru/WC_x and WC_x in 1.0 M KOH. (d) OH adsorption configurations on the Ru (001), WC_x, Ru site, and W site on Ru/WC_x and corresponding binding energies. (e) Projected densities of states (PDOS) of W 5d orbitals, Ru 4d orbitals, and O 2p orbitals for OH adsorption in W site and Ru site.

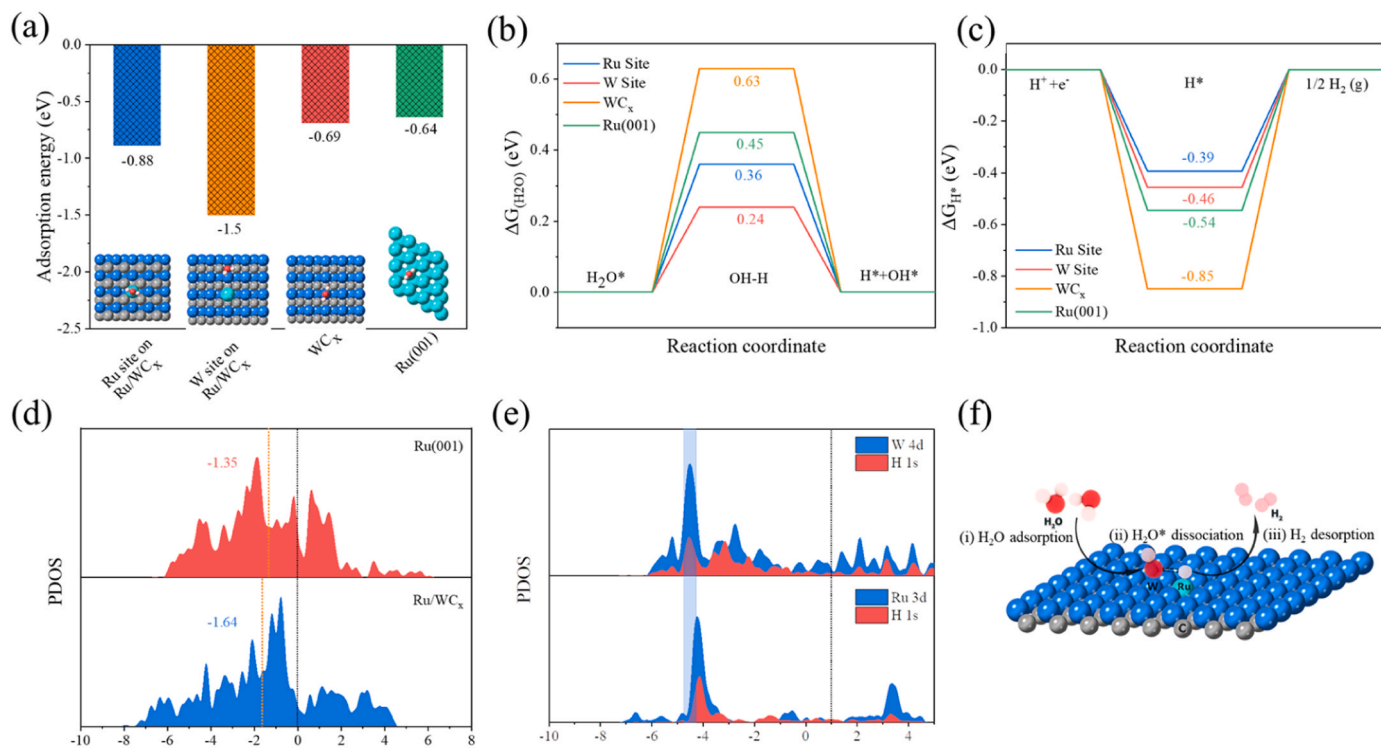


Fig. 5. DFT simulations of the HER processes on different catalysts. (a) Free energies of H₂O-adsorption for different models. (b) The free energy of water dissociation for different catalysts. (c) Gibbs free energy of H* adsorption for different catalysts. (d) The d-band of Ru in Ru (001) and Ru/WC_x. (e) The PDOS of W 5d orbitals, Ru 4d orbitals, and H 1s orbitals for H adsorption in the W site and Ru site. (f) Schematic mechanism for alkaline HER by efficiently splitting the HO-H bond on Ru-W sites of Ru/WC_x.

preferentially adsorbs and cleaves water molecules during alkaline HER but also effectively inhibits the poisoning of the active site by OH species, thus effectively facilitating the HER reaction.

From a thermodynamic point of view, DFT calculations were used to further elaborate the changes in the adsorption energies by taking WC_x crystal confined Ru for OH. Firstly, we constructed the Ru/WC_x model for Ru atoms doped with WC_x based on the experimental results, and the Ru (001), as well as WC_x model, was also constructed as a comparison. All models are in good agreement with experimental measurements (Figs. S25, S26 and S27). As illustrated in Fig. 4d, OH_{ad} is more favorably adsorbs on WC_x (−1.94 eV) compared to Ru (001) (−0.34 eV). The OH_{ad} adsorption energies of Ru site and W site in Ru/WC_x are −1.03 and −1.32 eV, respectively. This indicates that OH[−] will preferentially adsorb to the W site in HER reaction, which greatly alleviates the hydroxyl poisoning of the Ru active site. Furthermore, the calculation of the PDOS indicates that the 4d orbital of the Ru atom and the 5d orbital of the W atom and the 2p orbital of the oxygen atom have significant peak overlap below the Fermi energy level, respectively (Fig. 4e). The W-O peak shift is prominent to a lower energy level compared to the Ru-O peak, showing a stronger bonding. Therefore, it can be speculated that the OH in the electrolyte preferentially forms W-O bonds with the W in Ru/WC_x during the reaction, which agrees well with the experimental observations.

In light of the aforementioned findings, we further investigated the reaction barriers of the synthesized catalysts, including the Volmer step dissociation of the H₂O molecule and the subsequent conversion of H⁺ to H₂. Therefore, large H₂O adsorption energy, out-bound H₂O dissociation efficiency, and optimization of M-H bond energy are the main ways to enhance the performance of basic HER. The adsorption energy of water molecules on Ru (001), WC_x, and Ru site, and W site in Ru/WC_x were first calculated (Fig. S28). As shown in Fig. 5a, the H₂O adsorption energies of Ru and W sites in Ru/WC_x were −0.88 and −1.50 eV, respectively, which were significantly better than Ru (100) (−0.64 eV) and WC_x (−0.69 eV). It indicates that Ru/WC_x can adsorb H₂O molecules faster, which in turn accelerates the subsequent H₂O dissociation process. Notably, the more negative H₂O adsorption energy on the W site is determined by its smaller d-band center compared to the Ru site (Fig. S29). Then, the H₂O dissociation curves were calculated to further elucidate the catalytic behavior of the catalyst in alkaline media (Figs. S30, S31, S32 and S33). Specifically, WC_x has a large water dissociation potential energy (0.63 eV) indicating a slower HER kinetics in alkaline media [20]. In contrast, Ru/WC_x in the presence of Ru exhibits a lower H₂O dissociation energy barrier (Ru site on Ru/WC_x @0.36 eV and W site on Ru/WC_x @0.28 eV), which is significantly lower than Ru (100) (0.45 eV) (Fig. 5b). This result also demonstrates that Ru/WC_x has a faster proton supply rate in the alkaline medium HER process, thus speeding up the next Tafel or Heyrovsky step. The Gibbs free energy of hydrogen adsorption (ΔG_{H^*}) is the basic descriptor for determining the activity of HER [64,65], medium ΔG_{H^*} (~0) is essential for a high effective electrocatalyst to surmount the barriers of adsorption and desorption. Ru/WC_x exhibited the best hydrogen adsorption levels with −0.39 eV, −0.46 eV for Ru site and W site, respectively, while Ru (001) (−0.54 eV) and WC_x (−0.85 eV) had more negative values (Figs. 5c and S34). The d-band center was calculated to further explain the hydrogen adsorption free energy of the Ru site. Compared with the d-band electrons of Ru (001) (@−1.35), the active Ru in Ru/WC_x is far away from the Fermi energy level (@−1.46) due to the lattice confinement of WC_x, indicating that the H dissociation process in its HER reaction is boosted (Fig. 5d). In addition, the H adsorption PDOS results at Ru and W sites indicated that the strength of the Ru-H bond was more favorable to the H desorption process, which was consistent with the free energy calculation (Fig. 5e). Overall, the HER reaction process of Ru/WC_x is proposed in Fig. 5f, where the H₂O molecule first splits by adsorption on the WC_x substrate and generates H₂ at the Ru site, thus enhancing the overall HER activity.

4. Conclusion

In summary, we demonstrate a Ru single-atom doped WC_x (Ru/WC_x) catalyst with nanoislands structure as well as lattice confinement effect in order to mitigate the strong interaction between Ru active sites and OH_{ad}. The experimental and theoretical analyses indicated that the adsorbed hydroxyl poisoning effect of the Ru active site was effectively alleviated by the unique oxophilicity of the WC_x substrate. Additionally, W atoms as a reaction site significantly lowers the energy barrier for H₂O dissociation and ensures an adequate supply of protons, boosting the HER efficiency. The as-designed Ru/WC_x requires an ultralow overpotential of only 29 mV to drive a current density of 10 mA cm^{−2}, surpassing commercial Pt/C catalysts for basic HER. Furthermore, it can serve as an exceptionally efficient catalyst for HER in alkaline seawater. Importantly, the demonstrated competitive adsorption strategy offers fresh insights into the design of high-performance catalysts.

CRedit authorship contribution statement

Chen Xinyu: Conceptualization, Investigation, Methodology, Writing – original draft. **Zhang Kai:** Writing – review & editing. **Sun Bianjing:** Formal analysis, Funding acquisition, Supervision, Visualization, Writing – review & editing. **Sun Dongping:** Funding acquisition, Supervision. **Majeed Muhammad Amjad Muhammad:** Investigation, Visualization. **Chen Chuntao:** Formal analysis, Writing – review & editing.

Declaration of Competing Interest

The authors declare that they have no known competing financial interests or personal relationships that could have appeared to influence the work reported in this paper.

Data availability

Data will be made available on request.

Acknowledgement

This work was financially supported by the Fundamental Research Funds for the Central Universities (Grant 30920130121001), Project funded by Jiangsu Funding Program for Excellent Postdoctoral Talent, the National Natural Science Foundation of China (Grants 51873087).

Appendix A. Supporting information

Supplementary data associated with this article can be found in the online version at doi:10.1016/j.apcatb.2023.123644.

References

- [1] S. Chu, A. Majumdar, Opportunities and challenges for a sustainable energy future, *Nature* 488 (2012) 294–303.
- [2] Z.W. Seh, J. Kibsgaard, C.F. Dickens, I.B. Chorkendorff, J.K. Norskov, T. F. Jaramillo, Combining theory and experiment in electrocatalysis: insights into materials design, *Science* (355) (2017).
- [3] W.A. Bruff, J.M. Mueller, J.E. Trancik, Value of storage technologies for wind and solar energy, *Nat. Clim. Change* 6 (2016) 964–969.
- [4] R. Subbaraman, D. Tripkovic, K.-C. Chang, D. Strmcnik, A.P. Paulikas, P. Hirunsit, M. Chan, J. Greeley, V. Stamenkovic, N.M. Markovic, Trends in activity for the water electrolyser reactions on 3d M(Ni,Co,Fe,Mn) hydroxide catalysts, *Nat. Mater.* 11 (2012) 550–557.
- [5] M.S. Dresselhaus, I.L. Thomas, Alternative energy technologies, *Nature* 414 (2001) 332–337.
- [6] K. Jiang, M. Luo, Z. Liu, M. Peng, D. Chen, Y.-R. Lu, T.-S. Chan, F.M.F. de Groot, Y. Tan, Rational strain engineering of single-atom ruthenium on nanoporous MoS₂ for highly efficient hydrogen evolution, *Nat. Commun.* 12 (2021) 1687.
- [7] Y. Shi, Z.-R. Ma, Y.-Y. Xiao, Y.-C. Yin, W.-M. Huang, Z.-C. Huang, Y.-Z. Zheng, F.-Y. Mu, R. Huang, G.-Y. Shi, Y.-Y. Sun, X.-H. Xia, W. Chen, Electronic metal-support

- interaction modulates single-atom platinum catalysis for hydrogen evolution reaction, *Nat. Commun.* 12 (2021) 3021.
- [8] J.A. Turner, Sustainable Hydrogen Production, *Science* 305 (2004) 972–974.
 - [9] T.H. Wang, L. Tao, X.R. Zhu, C. Chen, W. Chen, S.Q. Du, Y.Y. Zhou, B. Zhou, D. Wang, C. Xie, P. Long, W. Li, Y.Y. Wang, R. Chen, Y.Q. Zou, X.Z. Fu, Y.F. Li, X. F. Duan, S.Y. Wang, Combined anodic and cathodic hydrogen production from aldehyde oxidation and hydrogen evolution reaction, *Nat. Catal.* 5 (2022) 66–73.
 - [10] H.Q. Fu, M. Zhou, P.F. Liu, P.R. Liu, H.J. Yin, K.Z. Sun, H.G. Yang, M. Al-Mamun, P. J. Hu, H.F. Wang, H.J. Zhao, Hydrogen spillover-bridged volmer/tafel processes enabling amperometric-level current density alkaline hydrogen evolution reaction under low overpotential, *J. Am. Chem. Soc.* 144 (2022) 6028–6039.
 - [11] K.L. Zhou, Z.L. Wang, C.B. Han, X.X. Ke, C.H. Wang, Y.H. Jin, Q.Q. Zhang, J.B. Liu, H. Wang, H. Yan, Platinum single-atom catalyst coupled with transition metal/metal oxide heterostructure for accelerating alkaline hydrogen evolution reaction, *Nat. Commun.* 12 (2021).
 - [12] H. Tan, B. Tang, Y. Lu, Q.Q. Ji, L.Y. Lv, H.L. Duan, N. Li, Y. Wang, S.H. Feng, Z. Li, C. Wang, F.C. Hu, Z.H. Sun, W.S. Yan, Engineering a local acid-like environment in alkaline medium for efficient hydrogen evolution reaction, *Nat. Commun.* 13 (2022).
 - [13] T. Zhang, J. Jin, J. Chen, Y. Fang, X. Han, J. Chen, Y. Li, Y. Wang, J. Liu, L. Wang, Pinpointing the axial ligand effect on platinum single-atom-catalyst towards efficient alkaline hydrogen evolution reaction, *Nature, Communications* 13 (2022) 6875.
 - [14] H. Zhang, Y. Wang, X. Li, K. Deng, H. Yu, Y. Xu, H. Wang, Z. Wang, L. Wang, Electrocatalytic upcycling of polyethylene terephthalate plastic to formic acid coupled with energy-saving hydrogen production over hierarchical Pd-doped NiTe nanoarrays, *Appl. Catal. B Environ.* 340 (2024), 123236.
 - [15] J. Zhang, T. Wang, P. Liu, Z.Q. Liao, S.H. Liu, X.D. Zhuang, M.W. Chen, E. Zschech, X.L. Feng, Efficient hydrogen production on MoNi₄ electrocatalysts with fast water dissociation kinetics, *Nat. Commun.* 8 (2017).
 - [16] D.W. Wang, Q. Li, C. Han, Q.Q. Lu, Z.C. Xing, X.R. Yang, Atomic and electronic modulation of self-supported nickel-vanadium layered double hydroxide to accelerate water splitting kinetics, *Nat. Commun.* 10 (2019).
 - [17] H. Huang, H. Jung, C.-Y. Park, S. Kim, A. Lee, H. Jun, J. Choi, J.W. Han, J. Lee, Surface conversion derived core-shell nanostructures of Co particles@RuCo alloy for superior hydrogen evolution in alkali and seawater, *Appl. Catal. B Environ.* 315 (2022), 121554.
 - [18] M. Wei, Y. Sun, F. Ai, S. Xi, J. Zhang, J. Wang, Stretchable high-entropy alloy nanoflowers enable enhanced alkaline hydrogen evolution catalysis, *Appl. Catal. B Environ.* 334 (2023), 122814.
 - [19] Y. Han, H. Duan, W. Liu, C. Zhou, B. Wang, Q. Jiang, S. Feng, W. Yan, T. Tan, R. Zhang, Engineering the electronic structure of platinum single-atom sites via tailored porous carbon nanofibers for large-scale hydrogen production, *Appl. Catal. B Environ.* 335 (2023), 122898.
 - [20] I.T. McCrum, M.T.M. Koper, The role of adsorbed hydroxide in hydrogen evolution reaction kinetics on modified platinum, *Nat. Energy* 5 (2020) 891–899.
 - [21] J. Mahmood, F. Li, S.-M. Jung, M.S. Okyay, I. Ahmad, S.-J. Kim, N. Park, H. Y. Jeong, J.-B. Baek, An efficient and pH-universal ruthenium-based catalyst for the hydrogen evolution reaction, *Nat. Nanotechnol.* 12 (2017) 441–446.
 - [22] Q. Zhou, Z. Wang, H. Yuan, J. Wang, H. Hu, Rapid hydrogen adsorption-desorption at sulfur sites via an interstitial carbon strategy for efficient HER on MoS₂, *Appl. Catal. B Environ.* 332 (2023), 122750.
 - [23] Q. He, Y. Zhou, H. Shou, X. Wang, P. Zhang, W. Xu, S. Qiao, C. Wu, H. Liu, D. Liu, S. Chen, R. Long, Z. Qi, X. Wu, L. Song, Synergic reaction kinetics over adjacent ruthenium sites for superb hydrogen generation in alkaline media, *Adv. Mater.* 34 (2022) 2110604.
 - [24] L. Li, H. Qiu, Y. Zhu, G. Chen, S. She, X. Guo, H. Li, T. Liu, Z. Lin, H. Zhou, Y. Zhu, M. Yang, B. Xu, H. Huang, Atomic ruthenium modification of nickel-cobalt alloy for enhanced alkaline hydrogen evolution, *Appl. Catal. B Environ.* 331 (2023), 122710.
 - [25] X.L. Jiang, H.S. Jang, S.G. Liu, Z.J. Li, M.G. Kim, C. Li, Q. Qin, X. Liu, J. Cho, The heterostructure of Ru₂P/WO₃/NPC synergistically promotes H₂O dissociation for improved hydrogen evolution, *Angew. Chem. Int. Ed.* 60 (2021) 4110–4116.
 - [26] J. Greeley, T.F. Jaramillo, J. Bonde, I. Chorkendorff, J.K. Nørskov, Computational high-throughput screening of electrocatalytic materials for hydrogen evolution, *Nat. Mater.* 5 (2006) 909–913.
 - [27] X. Chen, X.-T. Wang, J.-B. Le, S.-M. Li, X. Wang, Y.-J. Zhang, P. Radjenovic, Y. Zhao, Y.-H. Wang, X.-M. Lin, J.-C. Dong, J.-F. Li, Revealing the role of interfacial water and key intermediates at ruthenium surfaces in the alkaline hydrogen evolution reaction, *Nat. Commun.* 14 (2023) 5289.
 - [28] D.H. Kwon, M.S. Okyay, S.-J. Kim, J.-P. Jeon, H.-J. Noh, N. Park, J. Mahmood, J.-B. Baek, Ruthenium anchored on carbon nanotube electrocatalyst for hydrogen production with enhanced Faradaic efficiency, *Nat. Commun.* 11 (2020) 1278.
 - [29] S.Z. Zhou, H. Jang, Q. Qin, L.Q. Hou, M.G. Kim, S.G. Liu, X.E. Liu, J. Cho, Boosting hydrogen evolution reaction by phase engineering and phosphorus doping on Ru/P-TiO₂, *Angew. Chem. Int. Ed.* 61 (2022), e202212196.
 - [30] J. Kim, H. Jung, S.-M. Jung, J. Hwang, D.Y. Kim, N. Lee, K.-S. Kim, H. Kwon, Y.-T. Kim, J.W. Han, J.K. Kim, Tailoring binding abilities by incorporating oxophilic transition metals on 3D nanostructured Ni arrays for accelerated alkaline hydrogen evolution reaction, *J. Am. Chem. Soc.* 143 (2021) 1399–1408.
 - [31] J.J. Mao, C.T. He, J.J. Pei, W.X. Chen, D.S. He, Y.Q. He, Z.B. Zhuang, C. Chen, Q. Peng, D.S. Wang, Y.D. Li, Accelerating water dissociation kinetics by isolating cobalt atoms into ruthenium lattice, *Nat. Commun.* 9 (2018) 4958.
 - [32] C. Li, H. Jang, M.G. Kim, L.Q. Hou, J. Cho, Ru-incorporated oxygen-vacancy-enriched MoO₂ electrocatalysts for hydrogen evolution reaction, *Appl. Catal. B Environ.* 307 (2022), 121204.
 - [33] H. Song, M. Wu, Z. Tang, J.S. Tse, B. Yang, S. Lu, Single atom ruthenium-doped CoP/CDs nanosheets via splicing of carbon-dots for robust hydrogen production, *Angew. Chem. Int. Ed.* 60 (2021) 7234–7244.
 - [34] Y. Huang, X. Song, J. Deng, C. Zha, W. Huang, Y. Wu, Y. Li, Ultra-dispersed molybdenum phosphide and phosphosulfide nanoparticles on hierarchical carbonaceous scaffolds for hydrogen evolution electrocatalysis, *Appl. Catal. B Environ.* 245 (2019) 656–661.
 - [35] C. Cai, K. Liu, L. Zhang, F. Li, Y. Tan, P. Li, Y. Wang, M. Wang, Z. Feng, D. Motta Meira, W. Qu, A. Stefancu, W. Li, H. Li, J. Fu, H. Wang, D. Zhang, E. Cortés, M. Liu, Atomically local electric field induced interface water reorientation for alkaline hydrogen evolution reaction, *Angew. Chem. Int. Ed.* 62 (2023), e202300873.
 - [36] Y. Lu, Z. Zhang, H. Wang, Y. Wang, Toward efficient single-atom catalysts for renewable fuels and chemicals production from biomass and CO₂, *Appl. Catal. B Environ.* 292 (2021), 120162.
 - [37] Z. Ma, T. Wan, D. Zhang, J.A. Yuwono, C. Tsounis, J. Jiang, Y.-H. Chou, X. Lu, P. V. Kumar, Y.H. Ng, D. Chu, C.Y. Toe, Z. Han, R. Amal, Atomically dispersed Cu catalysts on sulfide-derived defective Ag nanowires for electrochemical CO₂ reduction, *ACS Nano* 17 (2023) 2387–2398.
 - [38] S. Li, B. Chen, Y. Wang, M.-Y. Ye, P.A. van Aken, C. Cheng, A. Thomas, Oxygen-evolving catalytic atoms on metal carbides, *Nat. Mater.* 20 (2021) 1240–1247.
 - [39] W. Wan, B.M. Tackett, J.G. Chen, Reactions of water and C1 molecules on carbide and metal-modified carbide surfaces, *Chem. Soc. Rev.* 46 (2017) 1807–1823.
 - [40] Y. Cui, X. Tan, K. Xiao, S. Zhao, N.M. Bedford, Y. Liu, Z. Wang, K.-H. Wu, J. Pan, W. H. Saputera, S. Cheong, R.D. Tilley, S.C. Smith, J. Yun, L. Dai, R. Amal, D.-W. Wang, Tungsten oxide/carbide surface heterojunction catalyst with high hydrogen evolution activity, *ACS Energy Lett.* 5 (2020) 3560–3568.
 - [41] Z. Chen, W. Gong, S. Cong, Z. Wang, G. Song, T. Pan, X. Tang, J. Chen, W. Lu, Z. Zhao, Eutectoid-structured WC/W₂C heterostructures: a new platform for long-term alkaline hydrogen evolution reaction at low overpotentials, *Nano Energy* 68 (2020), 104335.
 - [42] S.-C. Sun, F.-X. Ma, H. Jiang, M.-X. Chen, P. Xu, L. Zhen, B. Song, C.-Y. Xu, Encapsulating dual-phase WC-W₂C nanoparticles into hollow carbon dodecahedrons for all-pH electrocatalytic hydrogen evolution, *Chem. Eng. J.* 462 (2023), 142132.
 - [43] Z. Chen, Y. Xu, D. Ding, G. Song, X. Gan, H. Li, W. Wei, J. Chen, Z. Li, Z. Gong, X. Dong, C. Zhu, N. Yang, J. Ma, R. Gao, D. Luo, S. Cong, L. Wang, Z. Zhao, Y. Cui, Thermal migration towards constructing W-W dual-sites for boosted alkaline hydrogen evolution reaction, *Nat. Commun.* 13 (2022) 763.
 - [44] Q. Wang, M. Ming, S. Niu, Y. Zhang, G. Fan, J.-S. Hu, Scalable solid-state synthesis of highly dispersed uncapped metal (Rh, Ru, Ir) nanoparticles for efficient hydrogen evolution, *Adv. Energy Mater.* 8 (2018) 1801698.
 - [45] X. Zhang, M. Zhang, Y. Deng, M. Xu, L. Artiglia, W. Wen, R. Gao, B. Chen, S. Yao, X. Zhang, M. Peng, J. Yan, A. Li, Z. Jiang, X. Gao, S. Cao, C. Yang, A.J. Kropf, J. Shi, J. Xie, M. Bi, J.A. van Bokhoven, Y.-W. Li, X. Wen, M. Flytzani-Stephanopoulos, C. Shi, W. Zhou, D. Ma, A stable low-temperature H₂-production catalyst by crowding Pt on α -MoC, *Nature* 589 (2021) 396–401.
 - [46] S.T. Hunt, M. Milina, A.C. Alba-Rubio, C.H. Hendon, J.A. Dumesic, Y. Román-Leshkov, Self-assembly of noble metal monolayers on transition metal carbide nanoparticle catalysts, *Science* 352 (2016) 974–978.
 - [47] T. Zheng, C. Shang, Z. He, X. Wang, C. Cao, H. Li, R. Si, B. Pan, S. Zhou, J. Zeng, Interlayered iridium diselenide electrocatalysts for efficient pH-universal water splitting, *Angew. Chem. Int. Ed.* 58 (2019) 14764–14769.
 - [48] Y. Zhao, H. Cong, P. Li, D. Wu, S. Chen, W. Luo, Hexagonal RuSe₂ nanosheets for highly efficient hydrogen evolution electrocatalysis, *Angew. Chem. Int. Ed.* 60 (2021) 7013–7017.
 - [49] G. Kresse, J. Furthmüller, Efficient iterative schemes for ab initio total-energy calculations using a plane-wave basis set, *Phys. Rev. B* 54 (1996) 11169–11186.
 - [50] J.P. Perdew, K. Burke, M. Ernzerhof, Generalized gradient approximation made simple, *Phys. Rev. Lett.* 77 (1996) 3865–3868.
 - [51] S. Grimme, J. Antony, S. Ehrlich, H. Krieg, A consistent and accurate ab initio parametrization of density functional dispersion correction (DFT-D) for the 94 elements H-Pu, *J. Chem. Phys.* 132 (2010), 154104.
 - [52] L.-N. Zhang, Z.-L. Lang, Y.-H. Wang, H.-Q. Tan, H.-Y. Zang, Z.-H. Kang, Y.-G. Li, Cable-like Ru/WNO/C nanowires for simultaneous high-efficiency hydrogen evolution and low-energy consumption chlor-alkali electrolysis, *Energy Environ. Sci.* 12 (2019) 2569–2580.
 - [53] Y.-C. Chou, C.-Y. Wen, M.C. Reuter, D. Su, E.A. Stach, F.M. Ross, Controlling the growth of Si/Ge nanowires and heterojunctions using silver-gold alloy catalysts, *ACS Nano* 6 (2012) 6407–6415.
 - [54] B. Lu, L. Guo, F. Wu, Y. Peng, J.E. Lu, T.J. Smart, N. Wang, Y.Z. Finck, D. Morris, P. Zhang, N. Li, P. Gao, Y. Ping, S. Chen, Ruthenium atomically dispersed in carbon outperforms platinum toward hydrogen evolution in alkaline media, *Nat. Commun.* 10 (2019) 631.
 - [55] N. Chen, W. Zhang, J. Zeng, L. He, D. Li, Q. Gao, Plasma-Engineered MoP with nitrogen doping: Electron localization toward efficient alkaline hydrogen evolution, *Appl. Catal. B Environ.* 268 (2020), 118441.
 - [56] L. Zeng, Z. Zhao, Q. Huang, C. Zhou, W. Chen, K. Wang, M. Li, F. Lin, H. Luo, Y. Gu, L. Li, S. Zhang, F. Lv, G. Lu, M. Luo, S. Guo, Single-atom Cr-N₄ sites with high oxophilicity interfaced with Pt atomic clusters for practical alkaline hydrogen evolution catalysis, *J. Am. Chem. Soc.* 145 (2023) 21432–21441.
 - [57] Y. Guo, M. Wang, Q. Zhu, D. Xiao, D. Ma, Ensemble effect for single-atom, small cluster and nanoparticle catalysts, *Nat. Catal.* 5 (2022) 766–776.
 - [58] H. Huang, H. Jung, H. Jun, D.Y. Woo, J.W. Han, J. Lee, Design of grain boundary enriched bimetallic borides for enhanced hydrogen evolution reaction, *Chem. Eng. J.* 405 (2021), 126977.

- [59] Y. Zhu, K. Fan, C.-S. Hsu, G. Chen, C. Chen, T. Liu, Z. Lin, S. She, L. Li, H. Zhou, Y. Zhu, H.M. Chen, H. Huang, Supported ruthenium single-atom and clustered catalysts outperform benchmark Pt for alkaline hydrogen evolution, *Adv. Mater.* (2023), 2301133.
- [60] D. Cao, J. Wang, H. Xu, D. Cheng, Construction of dual-site atomically dispersed electrocatalysts with Ru-C₅ single atoms and Ru-O₄ nanoclusters for accelerated alkali hydrogen evolution, *Small* 17 (2021) 2101163.
- [61] J. Mao, C.-T. He, J. Pei, W. Chen, D. He, Y. He, Z. Zhuang, C. Chen, Q. Peng, D. Wang, Y. Li, Accelerating water dissociation kinetics by isolating cobalt atoms into ruthenium lattice, *Nat. Commun.* 9 (2018) 4958.
- [62] Y.-R. Hong, S. Dutta, S.W. Jang, O.F. Ngome Okello, H. Im, S.-Y. Choi, J.W. Han, I. S. Lee, Crystal facet-manipulated 2D Pt nanodendrites to achieve an intimate heterointerface for hydrogen evolution reactions, *J. Am. Chem. Soc.* 144 (2022) 9033–9043.
- [63] R. Subbaraman, D. Tripkovic, D. Strmcnik, K.-C. Chang, M. Uchimura, A. P. Paulikas, V. Stamenkovic, N.M. Markovic, Enhancing hydrogen evolution activity in water splitting by tailoring Li⁺-Ni(OH)₂-Pt interfaces, *Science* 334 (2011) 1256–1260.
- [64] T. Luo, J. Huang, Y. Hu, C. Yuan, J. Chen, L. Cao, K. Kajiyoshi, Y. Liu, Y. Zhao, Z. Li, Y. Feng, Fullerene lattice-confined ru nanoparticles and single atoms synergistically boost electrocatalytic hydrogen evolution reaction, *Adv. Funct. Mater.* 33 (2023) 2213058.
- [65] Y. Zheng, Y. Jiao, Y. Zhu, L.H. Li, Y. Han, Y. Chen, M. Jaroniec, S.-Z. Qiao, High electrocatalytic hydrogen evolution activity of an anomalous ruthenium catalyst, *J. Am. Chem. Soc.* 138 (2016) 16174–16181.